Inorganic Chemistry

Article

pubs.acs.org/IC

Structural Polymorphism in "Kesterite" Cu_2ZnSnS_4: Raman Spectroscopy and First-Principles Calculations Analysis

Mirjana Dimitrievska,*[,†,‡,§,¶] Federica Boero,[‖,¶] Alexander P. Litvinchuk,[⊥] Simona Delsante,[‖] Gabriella Borzone,[‖] Alejandro Perez-Rodriguez,[§,#] and Victor Izquierdo-Roca[§]

[†]National Renewable Energy Laboratory (NREL), Golden, Colorado 80401, United States

[‡]NIST Center for Neutron Research, National Institute of Standards and Technology, Gaithersburg, Maryland 20899-6102, United States

[§]Catalonia Institute for Energy Research (IREC), Jardins de les Dones de Negre, 1, 08930 Sant Adrià de Besòs, Barcelona, Barcelona, Spain

[‖]Department of Chemistry and Industrial Chemistry, University of Genoa, Via Dodecaneso 31, 16146, Genoa, Italy

[⊥]Texas Center for Superconductivity and Department of Physics, University of Houston, Houston, Texas 77204-5002, United States

[#]IN2UB, Universitat de Barcelona, C. Martí Franquès 1, 08028 Barcelona, Spain

Supporting Information

ABSTRACT: This work presents a comprehensive analysis of the structural and vibrational properties of the kesterite Cu_2ZnSnS_4 (CZTS, $I\bar{4}$ space group) as well as its polymorphs with the space groups $P\bar{4}2c$ and $P\bar{4}2m$, from both experimental and theoretical point of views. Multiwavelength Raman scattering measurements performed on bulk CZTS polycrystalline samples were utilized to experimentally determine properties of the most intense Raman modes expected in these crystalline structures according to group theory analysis. The experimental results compare well with the vibrational frequencies that have been computed by first-principles calculations based on density functional theory. Vibrational patterns of the most intense fully symmetric modes corresponding to the $P\bar{4}2c$ structure were compared with the corresponding modes in the $I\bar{4}$ CZTS structure. The results point to the need to look beyond the standard phases (kesterite and stannite) of CZTS while exploring and explaining the electronic and vibrational properties of these materials, as well as the possibility of using Raman spectroscopy as an effective technique for detecting the presence of different crystallographic modifications within the same material.

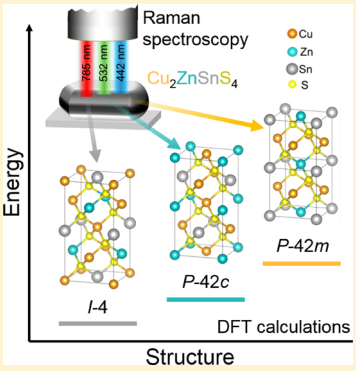

INTRODUCTION

Energy production from renewable processes has become increasingly important over the past few years. As such, photovoltaics are expected to play a significant role in meeting the rising demand of energy around the globe. Doing this in a sustainable way requires solar cells composed of earth-abundant, nontoxic, and cost-efficient materials. In that regard, kesterite structured pure sulfide Cu_2ZnSnS_4 (CZTS) has emerged as one promising alternative absorber layer for thin-film solar cells.[1−3]

CZTS has very suitable optical properties, such as a band gap of about 1.5 eV and a large absorption coefficient of up to about 10^4 cm^{-1} in the visible light region, and unlike the current state-of-the-art absorber $Cu(In,Ga)(S,Se)_2$ (CIGS), it does not contain any nonabundant elements.[4] However, the highest efficiency of CZTS reported to date is 8.4%,[5] which is far inferior to its thin-film counterparts. In order to achieve higher efficiency, a better understanding of CZTS device characteristics and performance is crucial. The main factor limiting the efficiency in CZTS is the open-circuit voltage,[6−8] which is significantly lower than the expected theoretical value, given the band gap. As the highest performing devices are usually made in Cu-poor and Zn-rich conditions,[9,10] one of the reasons for the poorer performance of CZTS-based solar cells is formation of secondary phases, such as ZnS and SnS, which can reduce the carrier transport and increase recombination.[11,12] Furthermore, nonstoichiometric conditions can lead to the coexistence of different stoichiometric structures or even disorder, which in general can have detrimental effects on the optoelectronic properties.[13−15]

In that regard, first-principles calculations have shown several candidate structures for CZTS that differ only slightly in energy. The kesterite structure ($I\bar{4}$) has proven to be the most stable, while the stannite ($I\bar{4}2m$) and two other tetragonal structural modifications of the kesterite structure ($P\bar{4}2c$ and $P\bar{4}2m$) are only slightly higher in energy (ΔE = 2.8 meV/atom for stannite, and ΔE = 3.2 meV/atom for $P\bar{4}2m$).[16,17] Identification of these structures with X-ray diffraction (XRD) is rather difficult, due to their similarity in the atomic scattering factors of Cu and Zn.[18,19] On the other side, Raman spectroscopy has proven to be a suitable technique in

Received: December 12, 2016
Published: March 6, 2017

ACS Publications © 2017 American Chemical Society

DOI: 10.1021/acs.inorgchem.6b03008
Inorg. Chem. 2017, 56, 3467−3474

identifying possible disorder in CZTS,[20,21] as well as secondary phases[11] and defects,[22] and as such should be able to differentiate individual structures of CZTS.

Previous studies have reported the vibrational frequencies of the three different CZTS structures ($I\bar{4}$, $I\bar{4}2m$, and $P\bar{4}2m$),[17,23,24] and recent works have also calculated the full Raman spectrum, including the intensities, for the kesterite, stannite, and $P\bar{4}2m$ phase.[17,25] However, no calculations of the vibrational properties or Raman experimental results have been presented on the $P\bar{4}2c$ structure, as well as any experimental confirmation on the possibility of the formation of these structures in the real material.

Early work of Schorr et al. has reported formation of a cubic sphalerite type of CZTS phase (space group $F\bar{4}3m$), which has been observed by neutron diffraction measurements after the phase transition of the kesterite CZTS at 876 °C.[26] However, from the theoretical point of view, arranging the cations of the CZTS phase in the lattice with $F\bar{4}3m$ symmetry should not be achievable, even though the experiments point in this direction. The discrepancy between experiment and theory in this case is actually due to the limitations of experimental methods and differences in the investigated volume of the material. As neutron and X-ray diffraction are macroscopic techniques, which probe the material on the millimeter scale, it is quite probable that on a macroscopic scale the investigated sample appeared to be isotropic cubic, while on a microscopic (several nanometers) scale it probably consists of several lower symmetry "distorted" phases. This is also the reason that samples that are treated at a high temperature are suitable candidates for investigating polymorph structures in the CZTS materials.

In this framework, this work describes a complete analysis and identification of all active Raman modes for CZTS polymorphs with $P\bar{4}2c$ and $P\bar{4}2m$ space groups using various excitation wavelengths. The experimental results compare well with the vibrational frequencies that have been computed by first-principles calculations based on density functional theory (DFT). These results can be used as a reference for future identification of the presence of these structures in the CZTS materials and its impact on solar cell performance.

EXPERIMENTAL SECTION

Material Preparation. In order to induce formation of the CZTS polymorph structure with the space group $P\bar{4}2c$, bulk crystalline CZTS samples with different starting compositions were prepared by a solid-state reaction method and subjected to different thermal treatments, as explained in ref 27. Samples with compositions along the ZnS–Cu_2SnS_3 section were prepared starting from the powders of the pure elements (Cu 99.999, Zn 99.9, Sn 99.999, and S 99.9995 mass %), weighed with an accuracy of at least ±0.5 mg. The powders were mixed, pressed into pellets, sealed in quartz glass ampules, and then subjected to the different thermal treatments.

The CZTS structural polymorphs ($P\bar{4}2c$ and $P\bar{4}2m$) were obtained from $Cu_{2-2x}Zn_{6+3x}Sn_{1-x}S_9$ samples subjected to a cyclic thermal treatment from 20 to 1100 °C with a 5°/min heating rate, then annealed at 700 °C for 15 days and quenched. At the end of the thermal treatment, a complete decomposition to ZnS + CZTS phases was observed, according to the eutectoidal reaction $Cu_{2-2x}Zn_{6+3x}Sn_{1-x}S_9 \leftrightarrows$ ZnS + CZTS, as proposed in ref 27.

Confirmation of the decomposition and formation of two separate phases (ZnS and CZTS) was obtained from the compositional analysis that was performed using an energy dispersive spectroscopy (EDS) detector and the Inca Energy software package (Oxford Instruments, Analytical Ltd., Bucks, U.K.).[28] For this analysis, the resin-mounted samples were prepared by grinding, lapping, and polishing with diamond abrasive spray down to 1 μm grain size. In order to detect the compositional contrast between the different phases, a backscattered electron (BSE) detector was used on a scanning electron microscope (SEM, Zeiss EVO 40). Figure 1 shows a SEM/EDX image of the investigated sample, with clear indication of the presence of two phases, ZnS and CZTS.

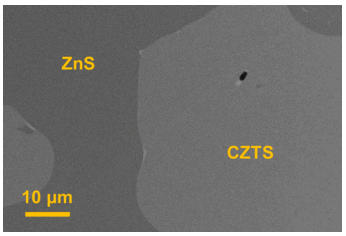

Figure 1. Surface SEM image of the bulk crystalline CZTS sample made with a BSE detector showing clear separation of two phases, ZnS and CZTS.

Characterization. Raman scattering measurements were performed in backscattering configuration using a custom-built Raman system coupled with an iHR320 Horiba Jobin Yvon spectrometer.[29] A detailed analysis was achieved using multiwavelength excitation Raman measurements combining UV (325 nm), blue (442 nm), green (532 nm), and red (633 nm) and near-infrared (785 nm) excitation lines. In all cases, and to avoid the presence of thermal effects in the spectra, the power excitation density was kept below 50 W/cm^2. To ensure the analysis of a representative area of each sample, measurements were made in macro configuration (laser spot size on the sample of ≥100 μm). The first-order Raman spectrum of monocrystalline Si was measured as a reference before and after acquisition of each Raman spectrum, and the spectra were corrected with respect to the Si line at 520 cm^{-1}. All Raman measurements were performed at room temperature with a spectral resolution of <2 cm^{-1}.

The synchrotron radiation powder XRD pattern for the as-synthesized CZTS sample was obtained on the Materials Science Beamline X04SA at the Swiss Light Source (transmission geometry in capillary, MYTHEN detector, λ = 0.563 564 Å) at the Paul Scherrer Institute.[30] The powder sample was loaded in a glass capillary, and all diffraction patterns were collected at room temperature. Structural refinements of all data were performed by the Rietveld method using the Full-Prof Suite program.[31]

Lattice Dynamics Calculations. The first-principles calculations of the electronic ground state of the Cu_2ZnSnS_4 kesterite-type structural modifications were performed within the generalized gradient approximation using the modified Perdew–Burke–Ernzerhof local functional PBESol,[32] as implemented in the CASTEP code.[33] Norm-conserving pseudopotentials were used. The cutoff energy for the plane wave basis was set to 800 eV. A self-consistent-field (SCF) tolerance better than 10^{-7} eV per atom and the phonon SCF threshold of 10^{-12} eV per atom were imposed. Prior to performing calculations, the structures were relaxed so that forces on atoms in the equilibrium position did not exceed 1 meV A^{-1} and the residual stress was below 5 × 10^{-3} GPa. The optimized crystal lattice parameters were found to be $a = b$ = 5.4479 Å, c = 5.4574 Å for the $P\bar{4}2m$ unit cell and $a = b$ = 5.4622 Å, c = 10.8731 Å for the $P\bar{4}2c$ cell. An integration over the Brillouin zone was performed over a 3 × 3 × 3 and 3 × 3 × 1 Monkhorst–Pack grid[34] in reciprocal space for the $P\bar{4}2m$ and $P\bar{4}2c$ structures, respectively. As it was recently shown for several quaternary semiconductors, Cu_2CdGeS_4,[35] Cu_2CdSiS_4,[35] and Cu_2ZnGeS_4,[36] the results of similar calculations agree very well with experimental data as far as symmetries and mode frequencies are concerned. Additionally, according to total energy calculations, kesterite was confirmed to be the ground state of CZTS, while $P\bar{4}2c$ and $P\bar{4}2m$ polymorphs possessed slightly higher energy by 1.7 and 7.8 meV, respectively.

All structural depictions were made using VESTA (Visualization for Electronic and Structural Analysis) software.[37]

DOI: 10.1021/acs.inorgchem.6b03008
Inorg. Chem. 2017, 56, 3467–3474

For all figures, standard uncertainties are commensurate with the observed scatter in the data, if not explicitly designated by vertical error bars.

RESULTS AND DISCUSSION

The kesterite $I\bar{4}$ structure and its polymorph modification $P\bar{4}2m$ contain 8 atoms in their primitive unit cell.[38,39] The

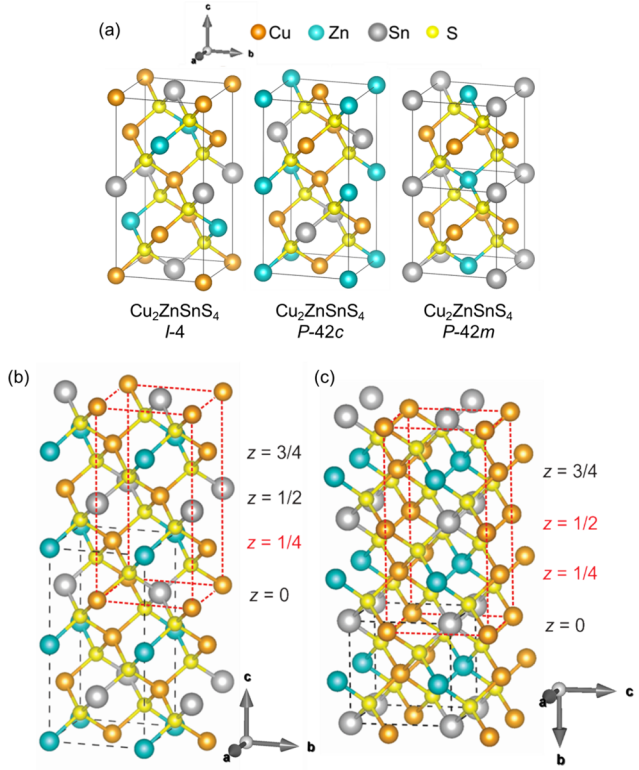

Figure 2. (a) Conventional unit cell representation of the tetragonal kesterite $I\bar{4}$ structure and its polymorphs of $P\bar{4}2c$ and $P\bar{4}2m$ modifications. Extended lattice of (b) the $P\bar{4}2c$ and (c) $P\bar{4}2m$ structures, allowing easier comparison with the kesterite $I\bar{4}$ structure. Differences in the atomic layers between the tetragonal kesterite $I\bar{4}$ structure and its polymorphs are labeled in red in (b) and (c).

conventional body-centered tetragonal unit cells of $I\bar{4}$ and $P\bar{4}2c$ space groups with 16 atoms are shown in Figure 1a. To facilitate the comparison, the $P\bar{4}2m$ structure is also shown in the same figure, consistent with two unit cells along the *c*-axis.

The structures consist of a *ccp* array of anions, with cations occupying one-half of the tetrahedral voids. Thus, the structures are closely related, but assigned to different space groups due to different distributions of the cations. In the case of the $I\bar{4}$ structure (No. 82), there are two inequivalent Cu atoms occupying Wyckoff positions at 2*a* (0, 0, 0) and 2*c* (0, 1/2, 1/4), while Zn and Sn atoms are located at 2*d* (0, 1/2, 3/4) and 2*b* (0, 0, 1/2) sites, respectively. This results in alternating cation layers of CuSn, CuZn, CuSn, and CuZn at z = 0, 1/4, 1/2, and 3/4, respectively. The S atoms are located on 8g (x, y, z) positions. On the other side, the $P\bar{4}2c$ structure (No. 112) represents tetragonal modification of the kesterite $I\bar{4}$ structure, where alterations are restricted to the exchange of Cu and Zn in the layer z = 1/4 of the cation sublattice. To facilitate the comparison, the $P\bar{4}2c$ structure was extended along the *c*-axis in Figure 2b. In this case, the two Cu atoms occupy 2*f* (1/2, 1/2, 0) and 2*b* (0, 1/2, 1/4) sites, while Zn resides in a 2*e* (0, 0, 0)

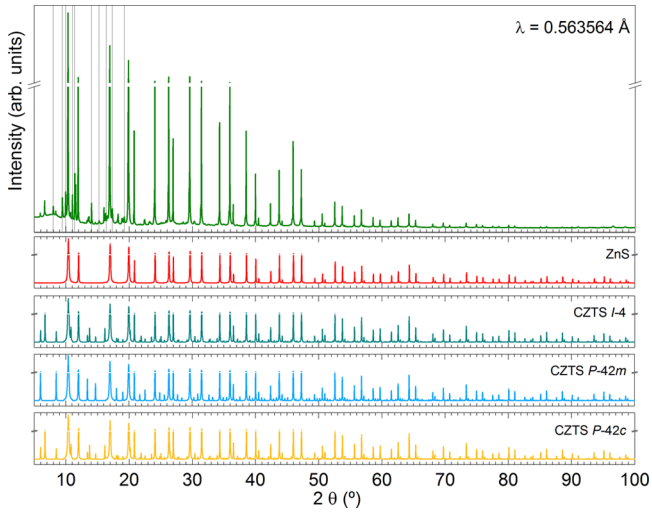

Figure 3. Comparison of the synchrotron XRD pattern of the prepared bulk crystalline CZTS sample (λ = 0.563 564 Å) and the reference patterns of ZnS and CZTS with the $I\bar{4}$, $P\bar{4}2m$, and $P\bar{4}2c$ structures simulated using parameters presented in Table S1 and S2 in the Supporting Information. Reflections marked with gray lines represent contributions from the SnS phase.

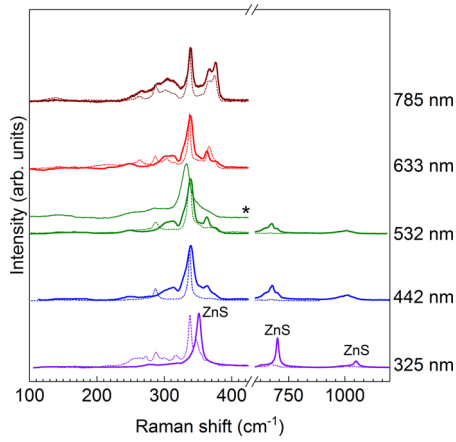

Figure 4. Raman spectra of the prepared bulk crystalline CZTS sample (full lines) in comparison to the measured Raman spectra of a reference CZTS polycrystalline thin film with the $I\bar{4}$ structure (dashed lines). The asterisk marks the Raman spectra of a CZTS sample with a low crystal quality.

position, and Sn in a 2*d* (1/2, 0, 1/4) site. The S anions are located on 8*n* (x, y, z) sites.

In the $P\bar{4}2m$ structure (No. 111), all the Cu atoms sit on 2*f* (1/2, 0, 1/2) sites, while the Zn and Sn atoms reside in 1*d* (1/2, 1/2, 0) and 1*a* (0, 0, 0) sites, respectively, and the S atoms occupy 4*n* (x, y, z) sites. This results in a primitive tetragonal structure with $c \approx a$. In comparison to the kesterite $I\bar{4}$ structure, in the $P\bar{4}2m$ modification Cu and Zn atoms are exchanged in the z = 1/4 layer, and Cu and Sn atoms are exchanged in the z = 1/2 layer (Figure 1c).

Figure 3 presents the synchrotron-measured XRD pattern of the CZTS sample. Rietveld refinement was used as a method for solving the structure of the studied CZTS. Refinements were performed using three starting structural models, each including a different CZTS polymorph structure ($I\bar{4}$, $P\bar{4}2m$, and $P\bar{4}2c$). Additionally, on analyzing the diffraction data, it became obvious that some impurities occur and have to be taken into

DOI: 10.1021/acs.inorgchem.6b03008
Inorg. Chem. 2017, 56, 3467−3474

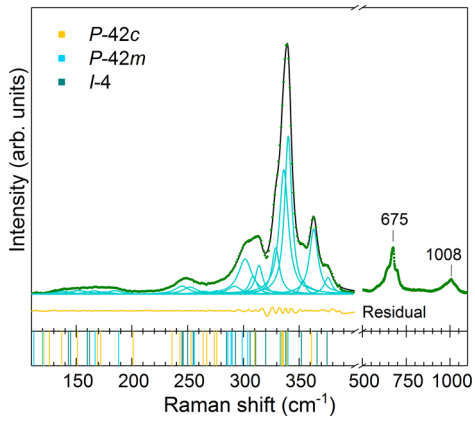

Figure 5. (Top) Deconvolution of the Raman spectra of the bulk crystalline CZTS sample measured with 532 nm excitation. The marked peaks represent second- and third-order Raman modes. (Bottom) Experimental Raman mode frequencies for the $I\bar{4}$ structure[40] and calculated Raman mode frequencies for the $P\bar{4}2c$ and $P\bar{4}2m$ structures.

account in the Rietveld analysis. In each case, two secondary phases were added: ZnS ($F\bar{4}3m$) and SnS ($Pnma$). The structural results of each refinement are summarized in Table S1 in the Supporting Information. The results showed that the fraction of SnS phase in all cases was <2%. The best refinement was obtained for the $P\bar{4}2c$ structure (Figure S1 in the Supporting Information); however, slightly worse χ^2-factors, as well as R_{Bragg} and R_{wp} values, obtained in the other two cases are not significant enough to completely disregard the presence of the other two structures in the sample. Additionally, very small differences in the unit cell parameters were found for the three crystal structures. This is due to the strong peak overlap among all three CZTS structures in the XRD pattern, as well as with ZnS, which causes difficulties in the refinement process and leads to correlation among the parameters. This is why the end results regarding structure are not reliable, and other structural characterizations must be made. As an example, Figure 3 presents the synchrotron-measured XRD pattern of the CZTS sample, with the reference patterns of the kesterite $I\bar{4}$ and its $P\bar{4}2c$ and $P\bar{4}2m$ modifications, as well as the ZnS secondary phase, which were simulated from parameters presented in Table S1 in the Supporting Information. Comparison of the most intense reflections for all CZTS structures results in an almost complete overlap. This is why XRD is not a suitable technique for identification of the CZTS polymorphs in the material.

Probing of these phases should be more easily achievable with Raman spectroscopy, as Raman spectra of different structures are expected to be rather distinct due to the variations in the vibrational displacements that are imposed by the symmetry of the lattice.

Figure 4 presents the experimental Raman spectra of the CZTS sample measured under different excitation wavelengths (full lines). Figure 4 also presents the Raman spectra (dashed lines) of a reference kesterite sample, with the $I\bar{4}$ structure, which has been previously reported in ref 40.

The appearance of the high-intensity peaks at around 350, 700, and 1050 cm^{-1} in the Raman spectra measured with UV excitation confirms the presence of the ZnS phase in the CZTS sample,[41] in agreement with the results obtained from the compositional EDX analysis. On the other side, measurements with the 442, 532, 633, and 785 nm excitations clearly show disagreement in the peak positions and the spectral shape between the kesterite $I\bar{4}$ structure and the measured data. In order to eliminate ZnS as a possible cause for the differences between the spectral shape of the measured CZTS sample and the reference CZTS, a separate study investigating the effect of ZnS on the Raman spectra measured with different excitation wavelengths was performed. In this case, separate CZTS thin films were prepared under Zn-rich conditions from the procedure presented by Fairbrother et al.[42] The imposed Zn excess led to formation of a ZnS secondary phase on the surface of the thin films. The films were then etched in a HCl solution for varying amounts of time (0, 90, and 300 s), which, as reported before,[42] selectively removes ZnS from the CZTS film surface until little ZnS is present (>300 s of etching). After each etching process, Raman spectra were measured using 325 and 532 nm excitation (Figure S3 in the Supporting Information). On the basis of the presented results, it can be observed that UV Raman spectra change drastically depending on the amount of ZnS present on the surface of the sample, while no changes are observed in the Raman spectra measured with 532 nm excitation. This is explained by the near-resonant Raman scattering behavior that is observed in the case of 325 nm excitation and due to the proximity of the ZnS optical band gap (3.66 eV) to the excitation wavelength (325 nm, 3.82 eV).[41] On the other side, as other used excitation wavelengths are significantly lower in energy (>442 nm, <2.8 eV) than the ZnS band gap, no resonant Raman scattering enhancement is expected, as ZnS is transparent at these wavelengths. Additionally, it should be noted that no traces of a SnS phase were observed in the Raman spectra, even though a small percentage of this phase was detected by XRD. This is expected, as previous studies usually report formation of this phase in the bulk of the material, rather than the surface.[11,43] These results suggest that the differences in the Raman spectra of the reference kesterite and the measured CZTS are caused by the differences in the structure, rather than the presence of the secondary phases.

Group theory analysis[38,39] predicts the following irreducible representation for the $I\bar{4}$ structure at the Γ point of the Brillouin zone: Γ = (1 B ⊕ 1 E) ⊕ (3 A ⊕ 6 B ⊕ 6 E), from which the 1 B and 1 E modes are acoustic modes, 3 A, 6 B, and 6 E are Raman-active modes, and only 6 B and 6 E are infrared-active modes. The A modes are expected to be the most intense peaks in the Raman spectra, as they involve only the anionic motion, and represent the signature peaks of the kesterite $I\bar{4}$ structure. The most intense A modes appear at 337 and 287 cm^{-1}, according to the previously reported data.[40,44,45] The absence of the second most intense mode at 287 cm^{-1} in the Raman spectra presented in Figure 4 indicates disruption of the $I\bar{4}$ symmetry in the crystal lattice. This could be caused either by the large quantity of defects leading to the lower crystalline quality of the material or by the rearrangement of the cations, leading to a new symmetry of the crystal lattice. The first case, of the increased quantity of defects, will cause significant broadening of all peaks in the spectra, which would be most noticeable in the A mode at 337 cm^{-1}.[21] An example of the Raman spectra measured on a low crystal quality CZTS sample[21] is presented in Figure 4 (marked with an asterisk). As can be seen, the spectrum corresponding to the low crystal quality CZTS does not match the measured Raman spectrum of the CZTS sample, indicating that the difference in the

DOI: 10.1021/acs.inorgchem.6b03008
Inorg. Chem. 2017, 56, 3467−3474

Table 1. Frequency (in cm^{-1}) of Peaks from Lorentzian Fitting of Raman Spectra Measured with Different Excitation Wavelengths and Proposed Mode Symmetry Assignment Compared with Theoretical Predictions for the $P\bar{4}2c$ and $P\bar{4}2m$ Structures and Reported Experimental Data from Refs 44 and 45[f]

CZTS sample (this work)		theoretical predictions (this work)						experimentally reported Raman modes (refs 44 and 45)	
		$P\bar{4}2c$			$P\bar{4}2m$			$I\bar{4}$	
ν [cm^{-1}][a]	assignment	ν [cm^{-1}][b]	sym[c]	activity[d]	ν [cm^{-1}][b]	sym[c]	activity[d]	ν [cm^{-1}][e]	sym[c]
		67	E	R/IR					
					71	B_2	R/IR		
		79	B_2	R/IR				83	E(TO+LO)
		80	E	R/IR				84	B(TO+LO)
		96	A_2	silent					
		96	E	R/IR	98	E	R/IR	98	E(TO+LO)
		105	B_1	R					
		121	E	R/IR	112	E	R/IR		
		126	A_2	silent	120	A_2	silent		
138.2	$P\bar{4}2c$	137	B_2	R/IR				143	E(TO)
152.4	$P\bar{4}2c$	151	E	R/IR				145	E(LO)
165.9	$P\bar{4}2c$/	162	B_1	R				160	B(TO)
	$P\bar{4}2m$/	169	B_2	R/IR	167	E	R/IR	162	B(LO)
	$I\bar{4}$								
176.2	$P\bar{4}2c$	172	E	R/IR					
184.7	$P\bar{4}2m$				188	B_2	R/IR		
201.4	$P\bar{4}2c$	201	E	R/IR					
233.7		236	B_2	R/IR					
244.9	$P\bar{4}2c$/	243	E	R/IR				245	B(TO)
	$I\bar{4}$								
252.1	$P\bar{4}2c$	250	B_1	R	256	E	R/IR	246	E(TO)
	$I\bar{4}$	253	E	R/IR				250	B(LO)
								255	E(LO)
264.3	$P\bar{4}2c$	**264**	**A_1**	**R**					
		264	B_1	R					
		267	E	R/IR					
277.0	$P\bar{4}2c$	274	B_2	R/IR					
		276	E	R/IR					
283.2	$P\bar{4}2c$/	**289**	**A_1**	**R**	286	B_1	R	**285**	**A**
	$P\bar{4}2m$/				289	B_2	R/IR		
	$I\bar{4}$				290	E	R/IR		
292.3	$I\bar{4}$				299	A_2	Silent	293	E(TO)
		304	A_2	silent					
301.5	$P\bar{4}2m$/				**304**	**A_1**	**R**	**306**	**A**
	$I\bar{4}$								
314.0	$I\bar{4}$							311	B(TO)
329.0	$P\bar{4}2m$/				333	E	R/IR	320	B(LO)
336.3	$P\bar{4}2c$/	**334**	**A_1**	**R**	338	B_2	R/IR	**338**	**A**
	$P\bar{4}2m$/	335	E	R/IR					
	$I\bar{4}$								
		336	A_2	silent					
340.3	$P\bar{4}2c$/	339	E	R/IR	**340**	**A_1**	**R**		
	$P\bar{4}2m$/	340	B_2	R/IR					
353.5	$I\bar{4}$							352	B(TO)
363.1	$P\bar{4}2c$	361	B_1	R				366	E(LO)
375.9	$I\bar{4}$							374	B(LO)

[a]Raman frequency obtained from the deconvolution. [b]Raman frequency obtained from the DFT calculations. [c]Mode symmetry. [d]Mode activity: R, Raman active; IR, infrared active; R/IR, Raman and infrared active. [e]Raman frequency experimentally reported in refs 44 and 45. [f]The most intense Raman modes are labeled in bold.

spectral shape and disappearance/appearance of certain peaks must originate from the changes in the lattice symmetry.

As Schorr et al. reported,[26] kesterite CZTS is expected to go through a phase transition at 876 °C, during which the tetragonal (ordered) CZTS phase ($I\bar{4}$) transforms gradually to the cubic sphalerite type of structure (temperatures higher than 888 °C). Upon cooling from these high temperatures, it is expected that, in addition to the kesterite $I\bar{4}$ structure, other tetragonal modifications could be formed. The main reason for this is the existence of the CZTS polymorphs, which are almost

DOI: 10.1021/acs.inorgchem.6b03008
Inorg. Chem. 2017, 56, 3467−3474

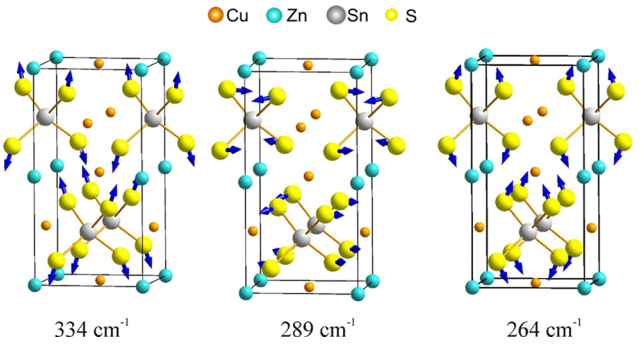

Figure 6. Calculated atomic displacement for the three A_1 modes of kesterite $P\bar{4}2c$ structure, with mode frequencies listed under each primitive cell.

degenerate in energy. Our DFT calculations have shown that after the $I\bar{4}$ structure $P\bar{4}2c$ has the lowest total energy among possible structures and, therefore, is most likely to form after the high-temperature treatment. Other possible structures, such as $P\bar{4}2m$ (No. 111), were also considered, although they have yielded higher energy minimums when compared to $P\bar{4}2c$ (by ΔE = 6.1 meV/atom in the case of $P\bar{4}2m$).

Group theory analysis predicts the following irreducible representation for the $P\bar{4}2c$ structure at the Γ point of the Brillouin zone: Γ = (1 B_2 ⊕ 1 E) ⊕ (3 A_1 ⊕ 5 B_1 ⊕ 6 B_2 ⊕ 13 E), from which 1 B_2 and 1 E mode are acoustic modes, 5 B_1 are silent modes, 3 A_1, 6 B_2, and 13 E are Raman-active modes, and only 6 B_2 and 13 E are infrared-active modes. Furthermore, an irreducible representation for the $P\bar{4}2m$ structure at the Γ point of the Brillouin zone is Γ = (1 B_2 ⊕ 1 E) ⊕ (2 A_1 ⊕ 2 A_2 ⊕ 1 B_1 ⊕ 4 B_2 ⊕ 6 E), from which 1 B_2 and 1 E mode are acoustic modes, 2 A_2 are silent modes, 2 A_1, 1 B1, 4 B_2, and 6 E are Raman-active modes, and only 4 B_2 and 6 E are infrared-active modes.

In order to resolve the symmetry of the formed structures in the CZTS sample, detailed deconvolution of the Raman spectra was performed with a minimum number of Lorentzian components, which led to a satisfying fit. A deconvoluted Raman spectrum of the CZTS sample measured with 532 nm excitation is presented in Figure 5.

Table 1 lists the Raman frequencies off all peaks obtained from the deconvolution, as well as the mode frequencies obtained from the DFT calculations for the $P\bar{4}2c$ and $P\bar{4}2m$ CZTS structures and the experimentally obtained mode frequencies of the $I\bar{4}$ CZTS structure. It should be noted that the TO/LO splitting has not been included in the calculations, and therefore the calculated frequencies present only the TO modes. However, including the TO/LO splitting would not impose significant changes in the mode frequencies, as based on the example of DFT calculations for kesterite,[24] only several of the of B and E symmetry modes might possess relatively large LO/TO splitting of 10 to 20 cm^{-1} (in the frequency range above 250 cm^{-1}), while other modes are only weakly polar and exhibit smaller splitting. Comparative analysis based on the intensity and the peak positions has led to the conclusion that the measured Raman spectra of the CZTS sample mostly correspond to the phase mixture with $P\bar{4}2c$ and $P\bar{4}2m$ polymorphs, with slight addition of the kesterite $I\bar{4}$ phase. Mixing of these phases is additionally confirmed by comparing in more detail the Raman spectra measured with 785 nm and other excitations (632, 532, and 442 nm). It can be observed that the 785 nm spectrum looks very similar to the reference spectrum of the $I\bar{4}$ structure, especially in the high-frequency region. On the other side, there are clear differences between the reference and the measured Raman spectra in the case of 632, 532, and 442 nm excitations. This is easily explained by the Raman resonance effects. The kesterite $I\bar{4}$ structure is resonant under 785 nm excitation, due to its band gap energy (1.5 eV) proximity to the laser excitation (1.58 eV), leading to enhancement in intensity of all polar modes (B and E).[40] This is why the spectrum of the CZTS sample measured with 785 nm excitation looks more like the Raman spectrum of the kesterite with $I\bar{4}$ structure. On the other side, the band gap energies of the $P\bar{4}2c$ and $P\bar{4}2m$ structures are expected to be lower, 1.4 and 1.2 eV, respectively, according to DFT calculations.[46] This means that no resonant effects are expected for the laser excitations of 442, 532, and 632 nm, and as such, modes corresponding to the $P\bar{4}2c$ and $P\bar{4}2m$ structures are expected to be dominant over the $I\bar{4}$ structure, as there is only a small fraction of the $I\bar{4}$ structure present in the sample.

Table 1 indicates a good match with the experimentally observed peaks and the theoretically predicted frequencies for the $P\bar{4}2c$ and $P\bar{4}2m$ structures. This is especially the case with the most intense A_1 modes. Minor disagreement in the Raman frequency between the experimental and the theoretical results is expected, due to approximations applied during the calculations.

The most intense A_1 modes in the $P\bar{4}2c$ and $P\bar{4}2m$ structures, corresponding to frequencies of 264, 284, and 300 cm^{-1}, could be used as an indicator of the presence of these phases in the material.

It is interesting to note that the three A_1 modes in the $P\bar{4}2c$ structure involve very different vibrational patterns when compared to the three A modes of the $I\bar{4}$ structure. While both types of modes involve only anion motion, the displacement patterns of the $I\bar{4}$ structure correspond to the SnS tetrahedra stretching, bending, and rotation about the *c*-axis, in order of decreasing mode frequency.[25,35] On the other hand, in the case of the $P\bar{4}2c$ structure, the three A_1 modes involve stretching, twisting, and bending of the SnS tetrahedra, in order of decreasing mode frequency (Figure 6). Apparently, this is a result of the lattice symmetry change, which imposes restrictions on the anion movement.

CONCLUSIONS

In conclusion, this work presents detailed theoretical and experimental characterization of different CZTS polymorphs (space groups: $I\bar{4}$, $P\bar{4}2c$, and $P\bar{4}2m$), in order to provide Raman spectra fingerprints as well as references for the different polymorph modifications. Bulk crystalline CZTS samples were prepared by the solid-state reaction method, undergoing thermal treatment, which favored the formation of the different polymorph structures. The samples were characterized by multiwavelength Raman scattering measurements using five different excitation wavelengths (325, 442, 532, 633, and 785 nm). Detailed deconvolution of the spectra with Lorentzian curves resolved 20 peaks, whose positions compared well with the vibrational frequencies computed by first-principles calculations based on density functional theory. Identification of the different structural polymorphs within the samples was made by comparative analysis using the experimental Raman spectra and the results from DFT calculations. Additionally, vibrational patterns of the most intense modes corresponding to the $P\bar{4}2c$ structure were calculated by DFT and compared with the corresponding modes in the $I\bar{4}$ CZTS structure. This

DOI: 10.1021/acs.inorgchem.6b03008
Inorg. Chem. 2017, 56, 3467−3474

work points to the need to look beyond the standard phases (kesterite and stannite) of CZTS when exploring and explaining the vibrational properties of these materials, as well as the possibility of using Raman spectroscopy as an effective technique for detecting the presence of different structures within the same material.

■ ASSOCIATED CONTENT

Supporting Information

The Supporting Information is available free of charge on the ACS Publications website at DOI: 10.1021/acs.inorgchem.6b03008.

Structural parameters, refinements, and additional Raman spectra (PDF)
Crystallographic data (CIF)
Crystallographic data (CIF)

■ AUTHOR INFORMATION

Corresponding Author

*E-mail: mira.dimitrievska@gmail.com; mirjana.dimitrievska@nist.gov, mirjana.dimitrievska@nrel.gov. Tel: +1 (301) 975-0403.

ORCID

Mirjana Dimitrievska: 0000-0002-9439-1019

Author Contributions

¶M. Dimitrievska and F. Boero contributed equally.

Notes

The authors declare no competing financial interest.

■ ACKNOWLEDGMENTS

M.D. gratefully acknowledges support from the U.S. DOE Office of Energy Efficiency and Renewable Energy, Fuel Cell Technologies Office, under Contract No. DE-AC36-08GO28308. A.P.L. acknowledges support from the State of Texas through the Texas Center for Superconductivity at the University of Houston. V.I.-R. and A.P.-R. acknowledge support from the SUNBEAM (ref. ENE2013-49136-C4-1-R) and NASCENT (ref. ENE2014-56237-C4-1-R) research projects from Spanish MINECO (Minsterio de Economía y Competitividad). The authors would like to thank Andrea Testino and Agnese Carino from the Paul Scherrer Institute for their help with the synchrotron measurements and their interpretation.

■ REFERENCES

(1) Liu, X.; Feng, Y.; Cui, H.; Liu, F.; Hao, X.; Conibeer, G.; Mitzi, D. B.; Green, M. The Current Status and Future Prospects of Kesterite Solar Cells: A Brief Review. *Prog. Photovoltaics* **2016**, *24*, 879−898.

(2) Katagiri, H. Cu2ZnSnS4 Thin Film Solar Cells. *Thin Solid Films* **2005**, *480*−*481*, 426−432.

(3) Wolden, C. A.; Kurtin, J.; Baxter, J. B.; Repins, I.; Shaheen, S. E.; Torvik, J. T.; Rockett, A. A.; Fthenakis, V. M.; Aydil, E. S. Photovoltaic Manufacturing: Present Status, Future Prospects, and Research Needs. *J. Vac. Sci. Technol., A* **2011**, *29*, 030801.

(4) Scragg, J. J.; Dale, P. J.; Peter, L. M. Towards Sustainable Materials for Solar Energy Conversion: Preparation and Photoelectrochemical Characterization of Cu_2ZnSnS_4. *Electrochem. Commun.* **2008**, *10*, 639−642.

(5) Shin, B.; Gunawan, O.; Zhu, Y.; Bojarczuk, N. A.; Chey, S. J.; Guha, S. Thin Film Solar Cell with 8.4% Power Conversion Efficiency Using an Earth-Abundant Cu_2ZnSnS_4 Absorber. *Prog. Photovoltaics* **2013**, *21*, 72−76.

(6) Tajima, S.; Asahi, R.; Isheim, D.; Seidman, D. N.; Itoh, T.; Hasegawa, M.; Ohishi, K. Atom-Probe Tomographic Study of Interfaces of Cu_2ZnSnS_4 Photovoltaic Cells. *Appl. Phys. Lett.* **2014**, *105*, 093901.

(7) Gunawan, O.; Todorov, T. K.; Mitzi, D. B. Loss Mechanisms in Hydrazine-Processed $Cu_2ZnSn(Se,S)_4$ Solar Cells. *Appl. Phys. Lett.* **2010**, *97*, 233506.

(8) Gokmen, T.; Gunawan, O.; Mitzi, D. B. Semi-Empirical Device Model for $Cu_2ZnSn(S,Se)_4$ Solar Cells. *Appl. Phys. Lett.* **2014**, *105*, 033903.

(9) Fairbrother, A.; Dimitrievska, M.; Sánchez, Y.; Izquierdo-Roca, V.; Pérez-Rodríguez, A.; Saucedo, E. Compositional Paradigms in Multinary Compound Systems for Photovoltaic Applications: A Case Study of Kesterites. *J. Mater. Chem. A* **2015**, *3*, 9451−9455.

(10) Mitzi, D. B.; Gunawan, O.; Todorov, T. K.; Wang, K.; Guha, S. The Path towards a High-Performance Solution-Processed Kesterite Solar Cell. *Sol. Energy Mater. Sol. Cells* **2011**, *95*, 1421−1436.

(11) Dimitrievska, M.; Fairbrother, A.; Saucedo, E.; Pérez-Rodríguez, A.; Izquierdo-Roca, V. Secondary Phase and Cu Substitutional Defect Dynamics in Kesterite Solar Cells: Impact on Optoelectronic Properties. *Sol. Energy Mater. Sol. Cells* **2016**, *149*, 304−309.

(12) Márquez, J.; Neuschitzer, M.; Dimitrievska, M.; Gunder, R.; Haass, S.; Werner, M.; Romanyuk, Y. E.; Schorr, S.; Pearsall, N. M.; Forbes, I. Systematic Compositional Changes and Their Influence on Lattice and Optoelectronic Properties of $Cu_2ZnSnSe_4$ Kesterite Solar Cells. *Sol. Energy Mater. Sol. Cells* **2016**, *144*, 579−585.

(13) Scragg, J. J. S.; Larsen, J. K.; Kumar, M.; Persson, C.; Sendler, J.; Siebentritt, S.; Platzer Björkman, C. Cu−Zn Disorder and Band Gap Fluctuations in $Cu_2ZnSn(S,Se)_4$: Theoretical and Experimental Investigations (Phys. Status Solidi B 2/2016). *Phys. Status Solidi B* **2016**, *253*, 189−189.

(14) Yin, X.; Tang, C.; Sun, L.; Shen, Z.; Gong, H. Study on Phase Formation Mechanism of Non- and Near-Stoichiometric $Cu_2ZnSn(S,Se)_4$ Film Prepared by Selenization of Cu−Sn−Zn−S Precursors. *Chem. Mater.* **2014**, *26*, 2005−2014.

(15) Hsu, W.-C.; Repins, I.; Beall, C.; DeHart, C.; To, B.; Yang, W.; Yang, Y.; Noufi, R. Growth Mechanisms of Co-Evaporated Kesterite: A Comparison of Cu-Rich and Zn-Rich Composition Paths. *Prog. Photovoltaics* **2014**, *22*, 35−43.

(16) Chen, S.; Gong, X. G.; Walsh, A.; Wei, S.-H. Crystal and Electronic Band Structure of Cu_2ZnSnX_4 (X = S and Se) Photovoltaic Absorbers: First-Principles Insights. *Appl. Phys. Lett.* **2009**, *94*, 041903.

(17) Ramkumar, S. P.; Gillet, Y.; Miglio, A.; van Setten, M. J.; Gonze, X.; Rignanese, G.-M. First-Principles Investigation of the Structural, Dynamical and Dielectric Properties of Kesterite, Stannite and PMCA Phases of Cu_2ZnSnS_4. *Phys. Rev. B: Condens. Matter Mater. Phys.* **2016**, DOI: 10.1103/PhysRevB.94.224302.

(18) Cheng, A.-J.; Manno, M.; Khare, A.; Leighton, C.; Campbell, S. A.; Aydil, E. S. Imaging and Phase Identification of Cu_2ZnSnS_4 Thin Films Using Confocal Raman Spectroscopy. *J. Vac. Sci. Technol., A* **2011**, *29*, 051203.

(19) Chen, S.; Walsh, A.; Luo, Y.; Yang, J.-H.; Gong, X. G.; Wei, S.-H. Wurtzite-Derived Polytypes of Kesterite and Stannite Quaternary Chalcogenide Semiconductors. *Phys. Rev. B: Condens. Matter Mater. Phys.* **2010**, *82*, 195203.

(20) Scragg, J. J. S.; Choubrac, L.; Lafond, A.; Ericson, T.; Platzer-Björkman, C. A Low-Temperature Order-Disorder Transition in Cu_2ZnSnS_4 Thin Films. *Appl. Phys. Lett.* **2014**, *104*, 041911.

(21) Dimitrievska, M.; Fairbrother, A.; Pérez-Rodríguez, A.; Saucedo, E.; Izquierdo-Roca, V. Raman Scattering Crystalline Assessment of Polycrystalline Cu_2ZnSnS_4 Thin Films for Sustainable Photovoltaic Technologies: Phonon Confinement Model. *Acta Mater.* **2014**, *70*, 272−280.

(22) Dimitrievska, M.; Fairbrother, A.; Saucedo, E.; Pérez-Rodríguez, A.; Izquierdo-Roca, V. Influence of Compositionally Induced Defects on the Vibrational Properties of Device Grade $Cu_2ZnSnSe_4$ Absorbers for Kesterite Based Solar Cells. *Appl. Phys. Lett.* **2015**, *106*, 073903.

(23) Gürel, T.; Sevik, C.; Çağın, T. Characterization of Vibrational and Mechanical Properties of Quaternary Compounds Cu_2ZnSnS_4 and

DOI: 10.1021/acs.inorgchem.6b03008
Inorg. Chem. 2017, 56, 3467−3474

$Cu_2ZnSnSe_4$ in Kesterite and Stannite Structures. *Phys. Rev. B: Condens. Matter Mater. Phys.* **2011**, *84*, 205201.
(24) Khare, A.; Himmetoglu, B.; Johnson, M.; Norris, D. J.; Cococcioni, M.; Aydil, E. S. Calculation of the Lattice Dynamics and Raman Spectra of Copper Zinc Tin Chalcogenides and Comparison to Experiments. *J. Appl. Phys.* **2012**, *111*, 083707.
(25) Skelton, J. M.; Jackson, A. J.; Dimitrievska, M.; Wallace, S. K.; Walsh, A. Vibrational Spectra and Lattice Thermal Conductivity of Kesterite-Structured Cu_2ZnSnS_4 and $Cu_2ZnSnSe_4$. *APL Mater.* **2015**, *3*, 041102.
(26) Schorr, S. The Crystal Structure of Kesterite Type Compounds: A Neutron and X-Ray Diffraction Study. *Sol. Energy Mater. Sol. Cells* **2011**, *95*, 1482−1488.
(27) Boero, F.; Delsante, S.; Colombara, D.; Borzone, G. A New Phase in the Cu−Sn−Zn−S Photovoltaic System. *Mater. Lett.* **2015**, *145*, 145−149.
(28) The mention of all commercial suppliers in this paper is for clarity. This does not imply the recommendation or endorsement of these suppliers by NIST.
(29) Dimitrievska, M.; Giraldo, S.; Pistor, P.; Saucedo, E.; Pérez-Rodríguez, A.; Izquierdo-Roca, V. Raman Scattering Analysis of the Surface Chemistry of Kesterites: Impact of Post-Deposition Annealing and Cu/Zn Reordering on Solar Cell Performance. *Sol. Energy Mater. Sol. Cells* **2016**, *157*, 462−467.
(30) Willmott, P. R.; Meister, D.; Leake, S. J.; Lange, M.; Bergamaschi, A.; Böge, M.; Calvi, M.; Cancellieri, C.; Casati, N.; Cervellino, A.; et al. The Materials Science Beamline Upgrade at the Swiss Light Source. *J. Synchrotron Radiat.* **2013**, *20*, 667−682.
(31) Rodriguez-Carvajal, J. *Fullprof: A Program for Rietveld Refinement and Pattern Matching Analysis*; Abstract of the Satellite Meeting on Powder Diffraction of the XV Congress of the IUCr, Toulouse, France, 1990; p 127.
(32) Perdew, J. P.; Ruzsinszky, A.; Csonka, G. I.; Vydrov, O. A.; Scuseria, G. E.; Constantin, L. A.; Zhou, X.; Burke, K. Restoring the Density-Gradient Expansion for Exchange in Solids and Surfaces. *Phys. Rev. Lett.* **2008**, *100*, 136406.
(33) Clark, S. J.; Segall, M. D.; Pickard, C. J.; Hasnip, P. J.; Probert, M. I. J.; Refson, K.; Payne, M. C. First Principles Methods Using CASTEP. *Z. Kristallogr. - Cryst. Mater.* **2009**, *220*, 567−570.
(34) Monkhorst, H. J.; Pack, J. D. Special Points for Brillouin-Zone Integrations. *Phys. Rev. B* **1976**, *13* (12), 5188−5192.
(35) Litvinchuk, A. P.; Dzhagan, V. M.; Yukhymchuk, V. O.; Valakh, M. Y.; Babichuk, I. S.; Parasyuk, O. V.; Piskach, L. V.; Gordan, O. D.; Zahn, D. R. T. Electronic Structure, Optical Properties, and Lattice Dynamics of Orthorhombic Cu_2CdGeS_4 and Cu_2CdSiS_4 Semiconductors. *Phys. Rev. B: Condens. Matter Mater. Phys.* **2014**, *90*, 165201.
(36) Guc, M.; Litvinchuk, A. P.; Levcenko, S.; Valakh, M. Y.; Bodnar, I. V.; Dzhagan, V. M.; Izquierdo-Roca, V.; Arushanov, E.; Pérez-Rodríguez, A. Optical Phonons in the Kesterite Cu_2ZnGeS_4 Semiconductor: Polarized Raman Spectroscopy and First-Principle Calculations. *RSC Adv.* **2016**, *6*, 13278−13285.
(37) Momma, K.; Izumi, F. *VESTA 3* for Three-Dimensional Visualization of Crystal, Volumetric and Morphology Data. *J. Appl. Crystallogr.* **2011**, *44*, 1272−1276.
(38) Aroyo, M. I.; Kirov, A.; Capillas, C.; Perez-Mato, J. M.; Wondratschek, H. Bilbao Crystallographic Server. II. Representations of Crystallographic Point Groups and Space Groups. *Acta Crystallogr., Sect. A: Found. Crystallogr.* **2006**, *62*, 115−128.
(39) Aroyo, M. I.; Perez-Mato, J. M.; Capillas, C.; Kroumova, E.; Ivantchev, S.; Madariaga, G.; Kirov, A.; Wondratschek, H. Bilbao Crystallographic Server: I. Databases and Crystallographic Computing Programs. *Z. Kristallogr. - Cryst. Mater.* **2009**, *221*, 15−27.
(40) Dimitrievska, M.; Fairbrother, A.; Fontané, X.; Jawhari, T.; Izquierdo-Roca, V.; Saucedo, E.; Pérez-Rodríguez, A. Multiwavelength Excitation Raman Scattering Study of Polycrystalline Kesterite Cu_2ZnSnS_4 Thin Films. *Appl. Phys. Lett.* **2014**, *104*, 021901.
(41) Dimitrievska, M.; Xie, H.; Jackson, A.; Fontané, X.; Espíndola-Rodríguez, M.; Saucedo, E.; Pérez-Rodríguez, A.; Walsh, A.; Izquierdo-Roca, V. Resonant Raman Scattering of ZnS_xSe_{1-x} Solid Solutions: The Role of S and Se Electronic States. *Phys. Chem. Chem. Phys.* **2016**, *18*, 7632−7640.
(42) Fairbrother, A.; García-Hemme, E.; Izquierdo-Roca, V.; Fontané, X.; Pulgarín-Agudelo, F. A.; Vigil-Galán, O.; Pérez-Rodríguez, A.; Saucedo, E. Development of a Selective Chemical Etch To Improve the Conversion Efficiency of Zn-Rich Cu_2ZnSnS_4 Solar Cells. *J. Am. Chem. Soc.* **2012**, *134*, 8018−8021.
(43) Jackson, A. J.; Walsh, A. Ab Initio Thermodynamic Model of Cu_2ZnSnS_4. *J. Mater. Chem. A* **2014**, *2*, 7829−7836.
(44) Guc, M.; Levcenko, S.; Bodnar, I. V.; Izquierdo-Roca, V.; Fontane, X.; Volkova, L. V.; Arushanov, E.; Pérez-Rodríguez, A. Polarized Raman Scattering Study of Kesterite Type Cu_2ZnSnS_4 Single Crystals. *Sci. Rep.* **2016**, *6*, 19414.
(45) Dumcenco, D.; Huang, Y.-S. The Vibrational Properties Study of Kesterite Cu_2ZnSnS_4 Single Crystals by Using Polarization Dependent Raman Spectroscopy. *Opt. Mater.* **2013**, *35*, 419−425.
(46) Paier, J.; Asahi, R.; Nagoya, A.; Kresse, G. Cu_2ZnSnS_4 as a potential photovoltaic material: A hybrid Hartree-Fock density functional theory study. *Phys. Rev. B: Condens. Matter Mater. Phys.* **2009**, *79*, 115126.

DOI: 10.1021/acs.inorgchem.6b03008
Inorg. Chem. 2017, 56, 3467−3474